LAWRENCE
LIVERMORE
NATIONAL
LABORATORY

LLNL-PROC-425278

# Detonation Failure in Small Cylindrical LX-17 Charges

*K. T. Lorenz, D. E. Hare, P. Vitello, P. C. Souers, R. Chambers and E. L. Lee*

**March 3, 2010**

2010 International Detonation Symposium
Coeur d'Alene, Idaho, United States
April 11-16, 2010

**Disclaimer**

# Detonation Failure in Small Cylindrical LX-17 Charges

K. Thomas Lorenz*, David E. Hare*, Peter Vitello*, P. Clark Souers, Ron Chambers and Edward L. Lee*

*Energetic Materials Center
Lawrence Livermore National Laboratory, Livermore, CA, 94550

**Abstract.** We have applied a new embedded fiber optic (EFO) diagnostic[13] to measure the on-axis wavefront velocity of a failing detonation. The EFO probe uses a 1.6 mm diameter fiber embedded on the centerline of the explosive assembly. This diagnostic monitors the Doppler-shifted light reflected off the shock front in the fiber. Travelling shock front velocities are measured with high temporal precision over a ~10-μs window. This is sufficient to observe the detailed front history as the explosive transitions from steady-state detonation through failure to attenuation of the shock wave in the unburned explosive. We report here our observations on cylindrical charges of LX-17 fabricated to diameters near the predicted failure diameter. The detonation fails in the smaller charges, but over a period of ~1-3 microseconds. The extent of the transition time between steady detonation and the onset of failure is expected to be extremely sensitive to the explosive formulation, testing conditions and model parameters.

## Introduction

Despite relatively high performance under steady-state conditions, triaminotrinitrobenzene (TATB) formulations[1] can still exhibit classically non-ideal behavior – significant temperature effects, long run-to-initiation distances, poor corner turning, and large front-curvature and failure diameters. These complex detonics make TATB-based explosives notoriously difficult to model. Many elegant experimental techniques have been employed to investigate initiation mechanisms and the detonation front structure in steady flow. These data have been used extensively over the last 20 years to develop sophisticated initiation and growth models.[2-5] Steady state behavior can be approximated using simpler models such as program burn. As for failure phenomena, size-effect data and failure diameters form the starting point for most failure models, and these data have become the most obvious means of generalizing an explosive's "non-ideality".

Campbell's careful size-effect study of PBX 9502 (95% TATB, 5% Kel-F) made an important contribution toward understanding failure dynamics in TATB.[6] Hill and coworkers added front curvature studies and correlated these to Campbell's data.[7-8] These data have been used to calibrate DSD wave propagation models of PBX 9502, and also serve as a necessary validation set for any modern reactive flow model of TATB.[7] Recent advances in radiographic techniques have provided investigators a window for viewing front profiles and dead zones in a variety of 2D and 3D geometries,[9-11] and can provide a non-invasive means of looking into the material during detonation failure. However, standard flash x-ray techniques acquire only a few snapshots per

experiment, and may suffer from poor contrast. Proton radiography improves both the contrast and the number of time elements that can be imaged, but this technique requires extensive infrastructure.[12]

In this study we have employed an embedded probe to study the failure dynamics of LX-17 (92.5% TATB, 7.5% Kel-F). This embedded fiber optic (EFO) diagnostic[13] can acquire a continuous velocity record of a traveling detonation front without severe perturbation of the flow. We have incorporated this probe into a geometry that allows continuous acquisition of centerline wavefront velocities during a failing detonation. Figure 1 shows a schematic of the test configuration for the assemblies fired in this study. This design uses a donor column of LX-17 to establish steady flow in the detonation front before it passes into the acceptor column. By using the same explosive in the donor and acceptor columns, we avoid overdriving the detonation in the smaller diameter acceptor. Front velocities are measured with high temporal precision over a ~10-μs time window. This is sufficient to observe the detailed front history as the explosive transitions from steady-state detonation through failure, and ultimately to an attenuating shock wave in the unburned LX-17.

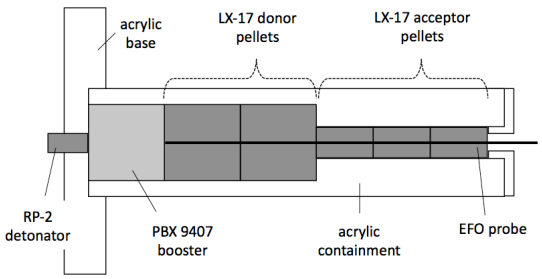


Fig. 1. Schematic of LX-17 failure test assembly with embedded fiber optic probe.

**Experimental Description**

Six shot assemblies were fabricated for this study. Donor columns, having diameters of 25.4 mm, consisted of an electric bridge-wire type detonator (RP-2, Teledyne; Tracy, CA), followed by a 25.4-mm long PBX 9407 (94% RDX, 6% VCTFE; LLNL Lot B-808) booster, and two 25.4-mm long LX-17 pellets. Three different acceptor diameters were used; 12.67, 10.12 and 7.57 mm. Boosters were hot die-pressed to an average density of 1.600 g/cc. All donor and acceptor pellets were pressed from LX-17-1 (LLNL Lot C-329) molding powder - formulated as 1-mm prill. The TATB crystals were synthesized using the wet-amination process, and sieve analysis gave a particle size distribution of: 27.75% under 20 μm and 71.29% under 45 μm. The pellets for the LX-17 donor column were hot-pressed using a special die set with a central pin to create a 1.60 mm diameter hole on their cylindrical axis. This hole provides a smooth, tight fit for the EFO probe. The average density (dimensional) for the donor columns was 1.910 g/cc, and the average radius was 25.34 mm. The donor column length was sufficient to achieve 99.5% the measured steady state value in this configuration,[13] and the front velocities at the donor-acceptor interface were repeatable to within 0.1%. The LX-17 pellets for the acceptor column were hot-pressed in standard dies of nominal diameters of 12.70 mm, 10.16 mm, and 7.62 mm. These had to have the probe holes drilled as a separate operation. We pressed parts with length-to-diameter ratios no greater than 2. This limits the number of pellet joints, but also the density gradients that can be generated in high aspect ratio pressed parts. The ~50 mm long acceptor columns were composed of 2, 3 and 4 pellets for the 12.67, 10.16 and 7.57 mm diameter columns, respectively. Average pellet densities and diameters are listed for each of the six shots in Table 1.

Table 1. LX-17 acceptor column specifications

| Shot Nos. | Diameter, mm | Density, g/cc |
|---|---|---|
| 232, 265 | 12.67, 12.66 | 1.913, 1.911 |
| 233, 266 | 10.12 | 1.914, 1.913 |
| 234, 267 | 7.57 | 1.910, 1.908 |

The EFO probe is a cladded fiber, having an aqueous CsCl solution-filled inner core with a polytetrafluoroethylene (PTFE) outer cladding. The inner core diameter is only 125 μm, and therefore the 1.6-mm diameter probe is treated as a one-piece PTFE fiber in our simulations. The velocimetry system used in these experiments is a

custom dual-cavity Fabry-Perot velocimeter equipped with a special Fabry-Perot filter to preferentially reduce the non-Doppler shifted component relative to the Doppler-shifted signal. This system has been previously described in some detail.[14] All shots were fired vertically in special stands. All had a thick confining sleeve machined out of a solid 50.8 mm diameter clear acrylic rod. The inside diameter of the acrylic confinement was custom reamed for each assembly to about 25 μm over the outside diameter of the explosive columns, and no attempt was made to fill this clearance. The small (~few microns) gap between the probe surface and the inner wall of the probe hole in the explosive sample was stemmed with distilled water. In our experience, a higher quality EFO record is obtained by using this water stemming. It is thought that the detonation wave in the explosive hydrodynamic couples more efficiently to the traveling shock wave in the probe with an intermediate layer of water rather than air.

**Experimental Results**

Initial design simulations using a reactive flow model suggested that the detonation would fail to propagate below ~12 mm for a rate column of LX-17 with an embedded PTFE fiber. Assemblies were then configured for acceptor columns having diameters that would be just above and below the expected failure diameter. Three diameters were chosen – one that was expected to propagate, and two that would fail. Figure 2 shows the detonation speed and shock speed history of six experiments (three diameters with duplicate shots) overlaid on a common time axis. Small differences in absolute timing can occur due to detonator jitter and donor column variations. Since we are comparing the dynamics in the smaller acceptor columns, the traces were temporally aligned so that the times when the detonation wavefront passed from the donor columns to the acceptor columns were coincident in all six shots. This was accomplished by overlapping the sharp dip in the traces at the 5-μs point. This is the junction between the two pellets in the donor columns. This signature is sharper than the velocity perturbation arising from the pellet junction at the end of the donor column, and is sufficient for temporally aligning the traces since the velocities in the last donor pellet are consistent for all six shots.

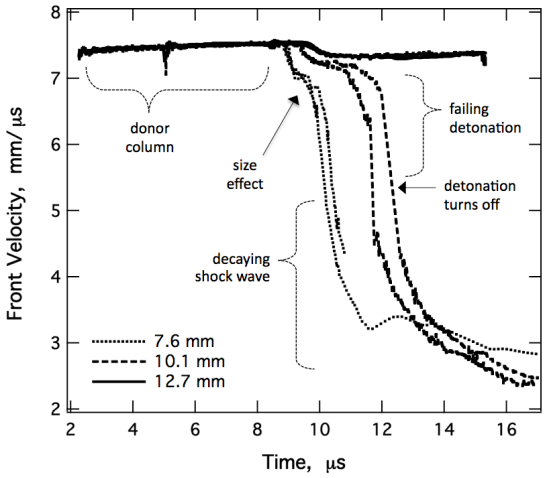


Fig. 2. Detonation-shock speed history of the six failure tests completed for this study.

With the six shots plotted on a common time axis, several features in the failure behavior stand out. For easy reference, we will refer to three dynamic regimes: prompt failure, quasi-steady propagation, and steady-state propagation. The detonation wave in the smallest diameter columns (7.6 mm) rapidly fails. Nonetheless, the EFO is able to capture some detail in this prompt failure. The velocity drops from ~7.5 mm/μs in the donor column to ~7 mm/μs, and then decreases rapidly to less than 3 mm/us. The "pause" in the failure near 7 mm/μs is a hint of the velocity that this size column would have if the wave could sustain steady propagation. This "size effect" is dynamically captured here in a column well below the failure diameter. The largest diameter acceptor column (12.7 mm) is above the failure diameter for this configuration (with a 1.6 mm embedded fiber). For this case, the wavefront velocity starts to decrease after 1-2 μs to ~7.3 mm/μs, but then propagates in steady state. The detonation wave in the intermediate size column (10.1 mm) achieves quasi-steady flow. After ~1 us, the flow velocity decrements to about 7.2 mm/μs and remains relatively steady for 1.5-2 μs. This quasi-steady state then transitions to a failing wave as seen in the "roll over" of the velocity. The velocity in the wavefront falls rapidly and then slows again and

finally levels out to the sound speed at ~2.5 mm/μs. This lower portion reflects the decaying shock wave in the unreacted LX-17 after the detonation turns off at ~5 mm/μs.

Figure 3 shows a Fabry-Perot interferogram for shot GGR 267 – one of the two 7.62-mm diameter charges. The contrast in this film record was modified and the aspect ratio was stretched in the horizontal (time) dimension for visual clarity. Velocities are tracked *via* fringes and fringe fiducials that are mirrored across a horizontal centerline in the film record. The data record begins at about the 2 μs mark and remains nearly steady until the 8.5 μs mark, which signifies the end of the donor column. After a short delay, the fringes bend down toward the central axis, decelerating into a failing detonation and finally to an attenuating shock wave. The interesting point to notice here is the film intensity of the record between the fringes. Note the darkened background between 2 and ~10 μs. This increased background intensity is due to broadband light emission entering the fiber and interferometer. The interferometer system has a filter that attenuates light that is outside the narrow frequency range of Doppler-shifted signal reflected from the traveling wavefront in the probe. Nonetheless, some of this light bleeds through the filter and darkens the film record. Note the strong termination of background darkening at the t = 10 μs point. We submit that this is due to the burning under the shock front "turning off", and the dynamics shifting to a dying shock wave. This point correlates approximately with the inflection point in the curvature of the velocity trace midway between the failing detonation wave and the decaying shock wave at 5-6 mm/μs. For the columns below the failure diameter, the background emission terminates at about the same time as the maximal fall in front velocity – somewhere between 5.2 and 5.7 mm/μs. The signal levels are noisy, but Figure 4 plots the two clearest representations of this phenomenon. The normalized background emission and velocities for GGR 234 (7.6 mm, triangle) and GGR 266 (10.1 mm, circle) are on a common time axis. The emission cut-off points are correlated with identical markers on the front velocity traces. For both cases the emission cut-off velocity is about 5.5 mm/us. We designate this as a velocity just above or at the failure point in the shock-initiated burning of LX-17, and it lies close to the inflection point between a failing detonation curve and a shock attenuation curve.

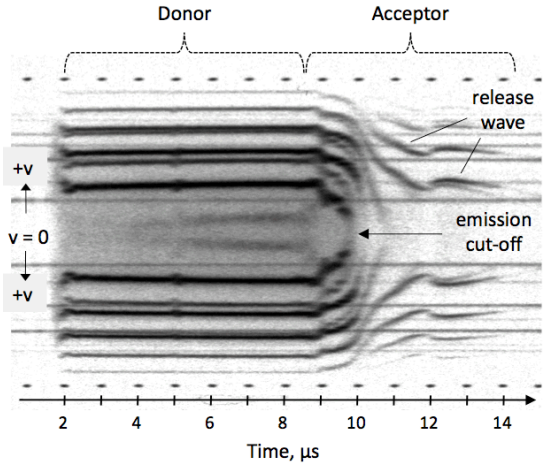


Fig. 3. Film record of Fabry-Perot velocity interferogram showing velocity fringes, release waves and background emission from the detonation process.

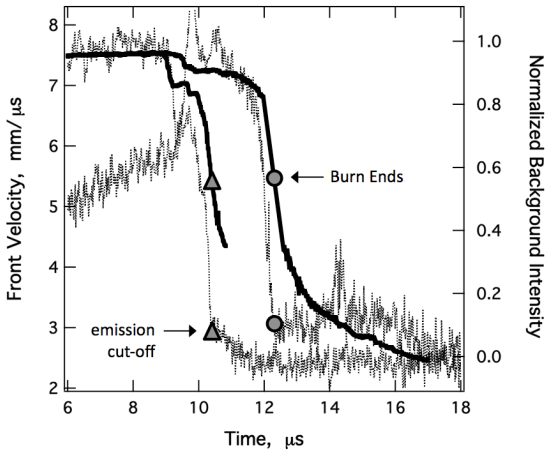


Fig. 4. Correlation of detonation failure to background emission in film records.

Finally, note that the two intermediate size shots showed a measurable difference in the quasi-steady dwell time – greater than the resolution of the experiment. This may be due to differences in the assemblies or the individual explosive samples, such as density, diameter, etc. No extraordinary efforts were made to generate near duplicate pellet

columns or assemblies. Improved density uniformity can be achieved by using samples cut from large pressed billets. Better shot-to-shot reproducibility may be achieved by using longer donor columns to achieve true steady state detonation. We are using modeling to provide an assessment of the sensitivity of the data to these experimental parameters. Simulations can then be folded back into revised designs for future experiments.

**Modeling and Discussion**

To aid in studying the kinetics of energetic material detonations the CHEETAH thermochemical code was coupled to a multi-dimensional Arbitrary Lagrangian Eulerian (ALE) hydrodynamic code.[5] In this scheme, CHEETAH is used to model the properties of chemically reacting flow in the high explosive, and the ALE code handles the hydrodynamic transport. CHEETAH solves thermodynamic equations between chemical species to find their equilibrium state, typically including 40-50 atomic, molecular, or condensed phase species. Fast reactions are assumed to be in instantaneous equilibrium while slow reactions are treated directly. The assumption of instantaneous equilibrium for fast reactions removes the need of specifying complex unknown reactions that are not time resolved in the modeling. The transformation of the high explosives into a reacting fluid of small product molecules is based on a simplified chemical kinetic rate scheme, whose coefficients were determined from fitting model results to measured detonation data. In modeling LX-17 for the simulations presented in this paper, we used two reaction rates. The first rate corresponds to the rapid burning of LX-17 to products. The second rate represents the slow growth of large graphite particles from small graphite particles. The LX-17 burn rate uses a Piece-Wise Linear (PWL) pressure dependent rate form, which allows for fine calibration adjustments.[4] The carbon kinetic rate is treated using the Arrhenius rate form. Calibration was done using both the data from this paper and other small-scale experiments. We call this calibrated PWL model the Tarantula model. Tarantula model simulations of the front velocities are over-plotted on the data in Figure 5. The simulations include the booster, donor and acceptor columns, and the acrylic containment. The fiber was modeled as a solid 1.6-mm diameter rod of PTFE. Model kinetics were calibrated to the later 10.1-mm diameter (GGR 266) shot data by adjusting the overall burn rate as well as the detailed shape of the PWL pressure dependent rate. Changes in the unreacted LX-17 equation of state were necessary to fit the low-velocity tail in the data. This calibrated model was then applied to the 7.6 and 12.7 mm diameter data.

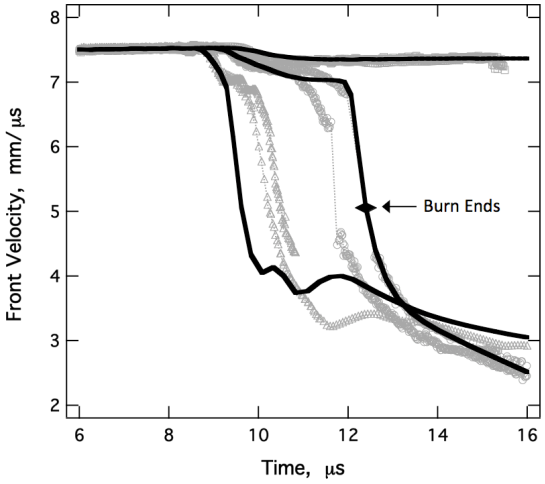


Fig. 5. Tarantula simulations of failure test data. The marker indicates where the model denotes the end of the burn process.

The overall fit to the data is quite acceptable. The run-up in the donor column is reproduced to within the experimental error. The steady-state velocity in the 12.7 mm diameter column was also reproduced. The shape of the failing detonations and shock attenuation curves are well modeled. However, the calibration could not simultaneously fit the 7.6 and 10.1 mm diameter data. The velocity "plateau" (near the 10 μs point) in the 7.6 mm data is not captured. And, there are details in the initial failure histories that could not be simulated by this model, despite significant efforts to adjust model parameters. Despite the imperfect fit to the data, this model should be able to reasonably assess the sensitivity of this geometry to various experimental and model parameters. Finally, the model predicts that reactive burn terminates at point where the velocity falls to ~5

mm/μs. This is similar to the point suggested by the background emission cut-off in Figure 4.

We evaluated the sensitivity and general behavior of this experimental geometry by adjusting the total burn rate in the model. This should determine which specific configurations are most sensitive to the detailed explosive characteristics that are often assessed – such as aging, density and formulation variations, and temperature dependent issues. Each of the three acceptor diameters were modeled using the calibrated burn rate, and perturbed rates of ±2%. Figure 6 shows results for this kinetics assessment.

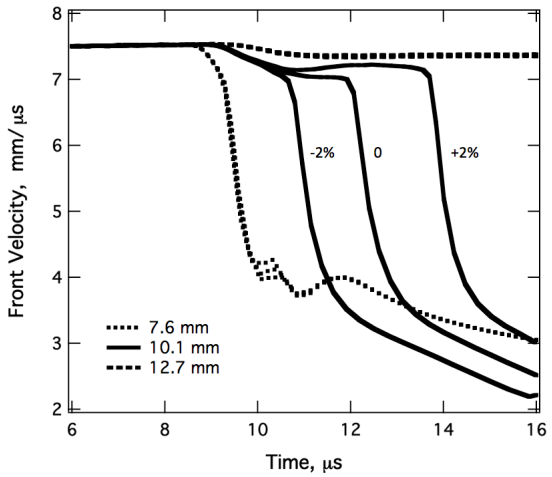


Fig. 6. Sensitivity of failure dynamics to small changes (±2%) in the model burn rate.

For the largest charge, a 2% adjustment has little or no effect on the steady detonation behavior. The same can be said for the smallest charge, except for some minor details in the low-velocity oscillations in the late stages of the dying shock wave. However, the same 2% burn rate adjustment has significant effects in the velocity history of the intermediate size charge. The decreased rate produces a 1.4 μs change in the time to failure, while the increased rate produces a 1.6 μs change. The prompt failure and steady state regimes are relatively insensitive to this level of kinetics variation. This modeling puts a bound on the sensitivity to kinetics for the quasi-steady regime. In this context, the two 10.1 mm data sets could be brought into coincidence by a 1.3% change in burn rate. Figure 7 depicts the affect of changes in charge diameter. Simulations were run for diameters of 6.4-14.0 mm, which span the range from prompt failure through steady state. Two model velocity histories for both small and intermediate diameters are shown in Fig. 7. In the prompt failure regime, a change in diameter of 2.7% generates a delay in failure time of 0.11 μs. However, a similar change in diameter (2.4%) in the quasi-steady regime generates a delay in failure time of 2.14 μs – nearly 20x greater. This shows the sensitivity of this new experimental geometry to the traditional diameter effect.

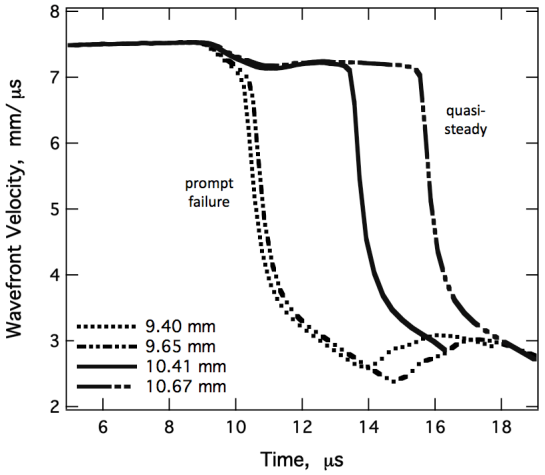


Fig. 7. The effect of charge diameter in two failure regimes – prompt failure and quasi-steady flow. Simulated velocity histories are shown for pairs of small and intermediate size charges.

By contrast, Fig. 8 demonstrates the relative insensitivity of model parameters to traditional size effect data. The open triangles present LX-17 rate stick data from LLNL cylinder tests. The solid and dashed lines show Tarantula simulations of these tests using the burn parameters from the GGR 266 calibration. The effect of a 2% change in burn rate is smaller than the variations in the cylinder test data. Note that these data and simulations have slightly higher velocities and an extended failure curve because they lack an embedded fiber and have additional confinement from copper sleeves. Hill and coworkers were able to observe lot differences in PBX 9502 front curvature and size effect data.[8] Extraordinary care

was taken to design and execute those rate stick experiments. We expect that this technique will prove to be more sensitive to performance variations due to lot variability. The steady and quasi-steady velocities from this study (solid squares) are also plotted in Fig. 8. The fiber occupies a small percentage of the cross sectional area in the donor charge, and therefore has only a small effect compared to a charge without an embedded fiber. However, the relative effect increases as the charge size decreases, reflected by the steepness of the trace with solid squares. Perhaps a more realistic comparison would be to plot these extracted quasi-steady velocities versus the reciprocal of the annular thickness (open squares) of the LX-17 in our acceptor column. The annular thickness equals the EFO radius minus the column radius. The data for an unconfined charge with no fiber would lie between this curve and the cylinder data. However, for the unconfined case, the curve would bend down sharply when the reciprocal radius exceeds ~0.25 $mm^{-1}$.

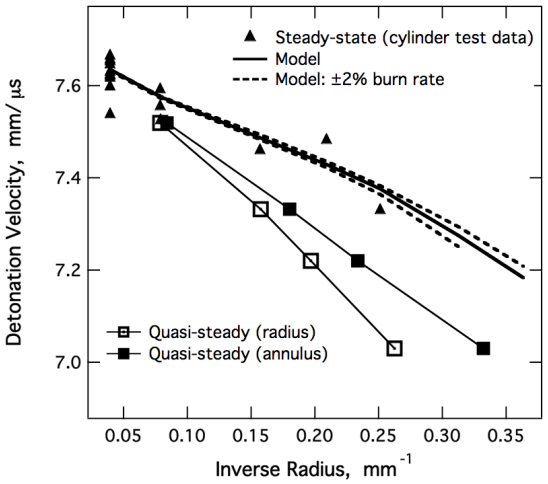


Fig. 8. LX-17 size effect: Tarantula modeling of cylinder test data showing sensitivity to kinetics. Steady and quasi-steady velocities (square symbols) from this study are included for comparison.

Using our newly calibrated burn model we can more precisely estimate the failure diameter for a bare cylindrical charge of LX-17. Figure 9 shows the velocity traces just above and below failure. Splitting the difference in these diameters, we estimate the failure diameter to be 8.25 mm. Campbell reported a failure diameter for PBX 9502 between 7.5 mm and 8 mm.[6] This is reasonable since PBX 9502 has 2.5% less binder than LX-17. For our configuration, we estimate the failure diameter to be 10.8 mm. The simulated velocities for charges having sizes close to the failure diameter (with an EFO) are also shown in Fig. 9. Note an additional effect between 10 μs and 12 μs. The front velocity in the fiber descends lower than the eventual steady or quasi-steady velocity. This is also observed in the experimental data. The front velocity in the 12.7 mm charges dips to 7.33 mm/μs and then rises steadily to 7.38 mm/us near the end of the acceptor column. A similar effect can be seen in the GGR 266 data, but the effect is poorly quantified for this charge size. The cause of this velocity minimum not yet understood. Despite the simple geometry and nice symmetry of the experiment, the model simulations suggest fairly complex wave interactions during failure.

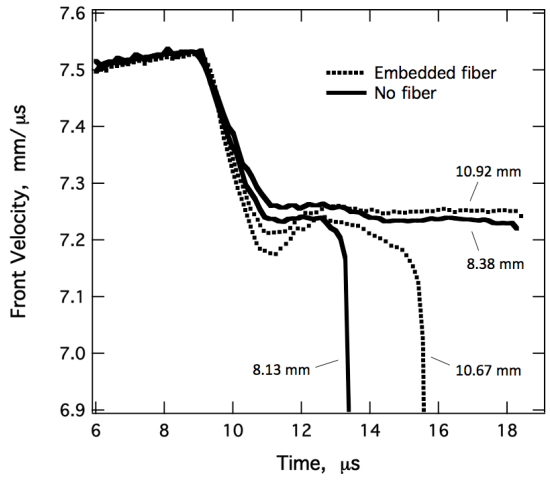


Fig. 9. Modeling the effects of the embedded fiber on the failure diameter. The velocity dip at the 10-μs point is suggestive of dynamics that are not yet understood.

The difficulty of closely matching the details in the EFO failure data is reflected in Fig. 10. This figure presents the data and calibrated simulations in the initial stages of failure as the detonation wave leaves the donor column and enters the acceptor column. The velocity histories are marked with

three time references (positioned in this case for events from the 12.7 mm charge data). $\tau_0$ is the donor-acceptor junction crossing time. $\tau_1$ is positioned at the time when the detonation velocity begins to decrease. This marks the point when the rarefaction wave originating at the charge edge reaches the charge axis. $\tau_2$ marks the time when the velocity stabilizes. The time difference between $\tau_1$ and $\tau_2$ reflects the equilibration time in the charge. This is the amount of time needed for the energy production and energy losses to effectively achieve parity in a charge moving to steady state flow. For our quasi-steady cases, this simple explanation is probably not sufficient to explain the existence and extent of the 1-2-μs long steady front velocities. Note also that the Tarantula simulations fall less rapidly to steady state flow than the data. The high-pressure sound speed in the reaction zone may be too low in the model.

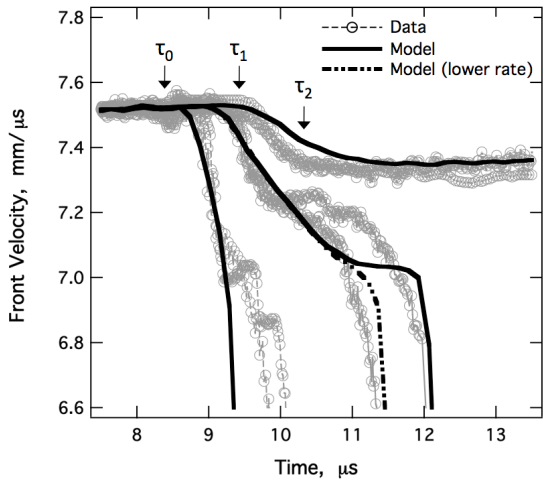


Fig. 10. Experimental and modeling features in the initial stages of failure.

Traditional size effect experiments treat failure as two-state phenomena – the charges either propagate or fail, without much additional information. This new experimental diagnostic allows us to assess the time-to-failure as a function of charge diameter. The time-to-failure is designated as the time for the detonation to fully extinguish. We suggested (Figs. 4 and 5) that this point was when the velocity fell to ~5 mm/μs. Figure 11 plots the calibrated model time-to-failure values as a function of charge diameter for our experimental configuration. A charge size above the failure diameter would have an infinite time-to-failure, and defines the asymptote for this curve. The model curve for non-propagating charge sizes exhibits two regions having differing slopes (or power laws). In the small-diameter (short failure time) section, the time-to-failure increases slowly and predictably with increasing charge diameter. We have labeled this section as the "prompt failure" regime. However, at a charge size of ~10 mm the failure behavior changes, and the slope increases in a clear fashion. In this region, small changes in charge diameter, kinetics or other parameters results in a large change in the time-to-failure. We labeled this section the quasi-steady regime, and this type behavior was exhibited by the intermediate (10.1 mm) diameter LX-17. Additional experimental work is needed to quantify this two-regime effect in LX-17. Tarantula simulations have shown that quasi-steady flow is a general characteristic of LX-17 failure dynamics. Continuous velocity measurements taken through the various stages of a failing detonation are suggestive of a new feature in TATB failure processes.

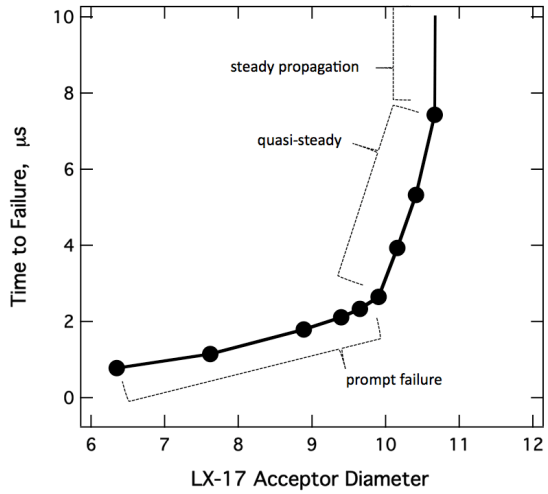


Fig. 11. Simulated time-to-failure for the embedded fiber failure test using calibrated Tarantula model. The time-size curve hints at two distinct failure regimes.

**Summary**

A new embedded fiber technique has been used to acquire continuous, time-resolved failure dynamics in LX-17. Detonation front velocities were tracked in charges above and below their failure diameter. Front velocity histories were divided into three distinct regimes: prompt failure, quasi-steady propagation and steady-state propagation. For charges below the failure diameter, the front transitioned from steady flow to a failing detonation wave and then to an attenuating shock wave. The detonation velocity at failure is estimated to be between 5.2 mm/μs and 5.7 mm/μs. Reactive flow simulations confirm the qualitative nature of burn termination at failure as well as the high sensitivity of this experimental geometry to important explosive parameters. Future plans call for temperature and compositional variations, as well as aging effects in TATB based formulations.

**Acknowledgements**

This work performed under the auspices of the U.S. Department of Energy by Lawrence Livermore National Laboratory under Contract DE-AC52-07NA27344.

**References**

1. Dobratz, B. M., "The insensitive high explosive triaminotrinitrobenzene (TATB): development and characterization – 1888 to 1994" *Los Alamos National Lab Report LA-13014-H*, 1995.

2. Souers, P. C., "JWL++: A simple reactive flow code package for detonation", *Propellants, Explosives and Pyrotechnics*, Vol. 25, p. 54, 2000.

3. Tarver, C. M. and McGuire, E. M., "Reactive flow modeling of the interaction of TATB detonation waves with inert material", *Proceedings of the 13th Detonation Symposium*, pp. 641-649, Norfolk, VA, July 2006.

4. Vitello, P. and Souers, P. C., The piecewise linear reactive flow rate model", *Proceedings of the 14th APS Topical Conference on Shock Compression of Condensed Matter*, Baltimore, MA, AIP Conf. Proc. 845, p. 507, 2006.

5. Vitello, P., Fried, L., Glaesemann, K. and Souers, C., "Kinetic Modeling of Slow Energy Release in Non-Ideal Carbon Rich Explosives", *Proceedings of the 13th Detonation Symposium*, pp. 465-475, Norfolk, VA, July 2006.

6. Campbell, A. W., "Diameter effect and failure diameter of a TATB-based explosive", *Propellants, Explosives and Pyrotechnics*, Vol. 9, pp. 183-187, 1984.

7. Hill, L. G., Bdzil, J. B. and Aslam, T. D., "Front curvature rate stick measurements and detonation shock dynamics calibration for PBX 9502 over a wide temperature range", *Proceedings of the 11th Detonation Symposium*, pp. 1029-1037, Snowmass, CO, August 1998.

8. Hill, L. G., Bdzil, J. B., Davis, W. C. and Critchfield, R. R., "PBX 9502 front curvature rate stick data: repeatability and the effects of temperature and material variation", *Proceedings of the 13th Detonation Symposium*, pp. 331-341, Norfolk, VA, July 2006.

9. Garcia, M. L. and Tarver, C. M., "Three-dimensional Ignition and Growth reactive flow modeling of prism failure tests on PBX 9502", *Proceedings of the 13th Detonation Symposium*, pp. 63-70, Norfolk, VA, July 2006.

10. Souers, P. C., et al., "LX-17 corner turning", *Propellants, Explosives and Pyrotechnics*, Vol. 29, p. 359, 2004.

11. Souers, P. C., et al., "LX-17 and PBX 9502 dead zones", *Propellants, Explosives and Pyrotechnics*, Vol. 31, p. 89, 2006.

12. Ferm, E. N. and Mariam, F., "Proton radiography observations of the failure of a detonation wave to propagate to the end of a conical explosive charge", *Proceedings of the 14th APS Topical Conference on Shock Compression of Condensed Matter*, Baltimore, MA, AIP Conf. Proc. 845, pp. 968-971, 2006.

13. Hare, D. E., Goosman, D. R., Lorenz, K. T. and Lee, E. L., "Application of the embedded fiber optic probe in high explosive detonation studies: PBX 9502 and LX-17", *Proceedings of the 13th Detonation Symposium*, pp. 1081-1091, Norfolk, VA, July 2006.

14. Goosman, D., Avara, G., Wade, J. and Rivera, A., “Optical Filters to Exclude Non-Doppler-Shifted Light in Fast Velocimetry” Lawrence Livermore National Laboratory report: UCRL-JC-145646-REV-1, 2002.